A modified many-body dissipative particle dynamics model for mesoscopic fluid simulation: methodology, calibration, and application for hydrocarbon and water

Qi Rao[a], Yidong Xia[a], Jiaoyan Li[b], Joshua McConnell[c], James Sutherland[c] and Zhen Li[d]

[a]Energy and Environment Science & Technology, Idaho National Laboratory, Idaho Falls, ID, USA; [b]Department of Mechanical and Aerospace Engineering, State University of New York at Buffalo, Buffalo, NY, USA; [c]Department of Chemical Engineering, University of Utah, Salt Lake City, UT, USA; [d]Department of Mechanical Engineering, Clemson University, Clemson, SC, USA

ARTICLE HISTORY

Compiled January 5, 2021

ABSTRACT

The many-body dissipative particle dynamics (mDPD) is a prominent mesoscopic multiphase model for fluid transport in mesoconfinement. However, it has been a long-standing challenge for mDPD (and other multiphase-enabled DPD models) to accurately predict real-fluid static and dynamic properties simultaneously. We have developed a modified mDPD model to overcome the issue and a rigorous calibration approach that uses reference data, including experimental and/or molecular dynamics (MD) simulations to parameterize the modified mDPD for real fluids. We choose heptane as a representative example of hydrocarbon in source rocks to demonstrate the model's capability to accurately predict the equation of state (EOS), free surface tension, diffusivity, and viscosity. Our timing test shows that the modified mDPD is 400-500 times faster than its MD counterpart for simulating bulk heptane in equivalent volumes. To further demonstrate the robustness of the model, we revisited the benchmark problem of mesoscopic modeling of water, in which all the previous

Corresponding author: Yidong Xia. Email: yidong.xia@inl.gov
Co-corresponding author: Zhen Li. Email: zli7@clemson.edu

works on DPD reported only a limited portion of the water properties. We show that the modified mDPD can provide accurate modeling of water static and dynamic properties and an EOS that matches the experimental data to a large range of confinement pressure.

KEYWORDS

Coarse graining; mesoscale; hydrocarbon; water; equation of state;

1. Introduction

Understanding the transport properties of hydrocarbons in mesoscale pores (i.e. with pore apertures that range from nanometers to micrometers) is important in the development of enhanced geotechnical engineering for energy source recovery and carbon capture & storage in low-porosity/permeability rock formations. To measure the hydrocarbon transport properties experimentally, however, is rather challenging, as the laboratory instrumentation for mesoscale confinement in in-situ geological conditions is still under development. With the growing capacity of computers, numerical modeling has been adopted as a complementary tool for those studies and for guiding the conceptual design of experiments. The choice of numerical models for fluids is normally based on their applicable space-time scales and computing costs, e.g., molecular dynamics (MD) models for tens of thousands of hydrocarbon molecules [1] and computational fluid dynamics (CFD) models in the continuum flow regime [2,3]. Those models, however, are either not computationally feasible (i.e. MD) or not theoretically capable (i.e. CFD) of resolving the fluid properties of interest in the mesoscale, for example, the equation of state (EOS), surface tension, diffusivity and viscosity. in the mesoscale. Those fluid properties can be strongly influenced by molecular diffusion and thermal fluctuations toward the lower range of mesoscale (i.e. a few nanometers), while behaving more similarly to continuum medium but with strong capillary effect toward the higher range of mesoscale (e.g., a few micrometers).

Dissipative particle dynamics (DPD) [4,5] is a class of mesoscopic fluid flow models that can potentially fill the gap between atomistic and macroscopic models. The theoretical foundation of DPD is established on the statistical mechanics [5,6]. The theory, methodology, developments, and applications of DPD are summarized in [7–9],

respectively. In the original DPD method, a cluster of fluid molecules are coarse-grained as a single bead. The atomistic interactions between fluid molecules are coarse-grained by simplified bead-bead interactions. The formulation of DPD also allows more structural complexities and constraints such as bond and dihedral, e.g., the red blood cell models [10–13]. As a result of coarse-graining from MD, the critical timestep in DPD models can be orders of magnitude larger than their MD counterpart and permit the sampling of both length and time scales equivalent to those experimentally measurable, though at the expense of neglecting the details of individual molecular interactions. In DPD, simulations of multiphase fluid dynamics have been made possible by a number of model variants [14–20]. Among those multiphase-enabled DPD models, the many-body DPD (mDPD) model [14] is a prominent candidate for mesoscopic simulations of fluid transport in mesoporous rock formations [21,22]. The mDPD model is suitable to model the EOS of liquid fluids by considering the many-body interactions [14,23–26] and has been applied in mesoscale simulations of liquid surface tension [27], contact angle characterization [28], and multiphase flow in micro-channels [29–31]. The formulation of mDPD assumes an isothermal condition in which the conservation of total energy is dismissed. This indicates that the mDPD model with calibrated parameters are valid only for a specific or narrow range of temperature. To model non-isothermal flow, the mDPD model requires additional constraint for total energy conservation [32–35], e.g. the recent work of [36], which is though not in the scope of the present study. We would like to note that none of the multiphase-enabled DPD models was devised to explicitly model the liquid-vapor coexistence. Those models, including mDPD, can be calibrated to accurately model the free surface tension of bulk liquids but not the properties of the gaseous phase. This limitation has been well discussed in [18], where the phenomena of liquid-vapor coexistence were simulated without guaranteeing the quantitative accuracy of vapor densities.

Despite the effectiveness of the mDPD model in the qualitative study of hydrocarbon transport and hydrocarbon-water interaction behavior in mesopores [21,22,29–31], it has been a long-standing challenge for researchers to make mDPD capable of reproducing the real fluid static properties (e.g. surface tension) and dynamic properties (diffusivity, viscosity, etc.) at the same time for fluids of interests, if not impossible. For

example, [10] calibrated the mDPD model to simulate the behavior hydrocarbon fluids in pores by only roughly fitting the hydrophilic and hydrophobic patterns of contact angles with confining walls. [37,38] only calibrated the fluid diffusivity whereas [31,39] only calibrated the fluid viscosity. All the previous calibration approaches that attempt to fit surface tension and fluid density will result in the model parameters that are different than those obtained by matching fluid compressibility [39]. Above all, how to accurately predict the fluid properties of hydrocarbons with the mDPD model is relatively unexplored but essential for mDPD to qualify for high-fidelity predictions of hydrocarbon transport properties in mesoporous confinement.

This work has developed a modified mDPD model by introducing a new independent degree of freedom (dissipative force cut-off radius decoupled from the conservative force cut-off radius) in the original mDPD model by [14] to enable the model to achieve accurate predictions of bulk EOS, surface tension, diffusivity and viscosity of real fluids. A rigorous calibration approach that uses reference data, including experimental and/or MD simulation results, is introduced to parameterize the modified mDPD for fluids of interest. Numerical examples are presented for the accurate modeling of the fluid properties of heptane (C_7H_{16}), as it is a representative hydrocarbon fluid in source rocks. Our numerical results show that upon a rigorous calibration, the modified mDPD model accurately predicts the EOS and key material properties including bulk density, compressibility, surface tension, diffusivity and viscosity. Our timing test shows that the modified mDPD model is over two orders of magnitude faster than its MD counterpart for simulations of bulk heptane in equivalent volumes, indicating the suitability of the model for accurate and efficient simulations of fluid transport at mesoscale. In addition, to demonstrate the robustness of the modified mDPD model, we revisited the benchmark problem of mesoscopic modeling of water, in which previous literature predicted a very limited portion of water properties with mDPD [27]. We report that the modified mDPD model is the first one in the class of DPD models that is capable of providing an accurate prediction of a much broader extent of the liquid water static and dynamic properties.

Above all, the novelties of this work are summarized in four aspects: 1) a modified model for mDPD is developed to enable the accurate prediction of fluid properties for

real fluids in the mesoscale; 2) a rigorous calibration approach is developed to enable the systematic parameterization of mDPD for fluids of interest; 3) it is shown that the modified mDPD model delivers high-fidelity prediction of hydrocarbon fluid properties, in which heptane is used as a representative example for its importance in subsurface energy source recovery; 4) the benchmark problem of mesoscopic modeling of water is revisited to demonstrate the robustness of the modified mDPD model to accurately model all the major fluid properties of liquid water, which is the first time with a DPD-based model.

The rest of this paper is organized as follows. The formulations of DPD and mDPD are introduced in Section 2. In Section 3, we describe a modified mDPD model for heptane-silica system and calibration approach for the model. Section 4 reports the application of the modified mDPD for heptane and water, followed by our summary and conclusions in Section 5.

2. DPD formulation

2.1. The original DPD

In a generic formulation, DPD particles interact via pairwise central forces, i.e.

$$\mathbf{F}_{ij} = \mathbf{F}_{ij}^{\mathrm{R}} + \mathbf{F}_{ij}^{\mathrm{D}} + \mathbf{F}_{ij}^{\mathrm{C}}, \tag{1}$$

where $\mathbf{F}_{ij}^{\mathrm{R}}$ represents a random force, $\mathbf{F}_{ij}^{\mathrm{D}}$ a dissipative force, and $\mathbf{F}_{ij}^{\mathrm{C}}$ a conservative force between particle i and j, respectively. If $\mathbf{r}_i$ and $\mathbf{v}_i$ are used to denote the position and velocity of particle i, respectively, the random force $\mathbf{F}_{ij}^{\mathrm{R}}$ and the dissipative force $\mathbf{F}_{ij}^{\mathrm{D}}$ can be expressed as

$$\mathbf{F}_{ij}^{\mathrm{R}} = \sigma w^{\mathrm{R}}(r_{ij})\xi_{ij}\hat{\mathbf{r}}_{ij} \tag{2}$$

and

$$\mathbf{F}_{ij}^{\mathrm{D}} = -\gamma w^{\mathrm{D}}(r_{ij})(\hat{\mathbf{r}}_{ij} \cdot \mathbf{v}_{ij})\hat{\mathbf{r}}_{ij} \tag{3}$$

respectively, where $\mathbf{r}_{ij} = \mathbf{r}_i - \mathbf{r}_j$, $r_{ij} = |\mathbf{r}_{ij}|$, $\hat{\mathbf{r}} = \mathbf{r}_{ij}/r_{ij}$ and $\mathbf{v}_{ij} = \mathbf{v}_i - \mathbf{v}_j$. These forces constitute a thermostat if the amplitude σ of the random variable ξ_{ij} and the viscous dissipation coefficient γ satisfy a fluctuation-dissipation theorem:

$$\sigma^2 = 2\gamma k_B T \tag{4}$$

and

$$w^{\mathrm{D}}(r) = (w^{\mathrm{R}}(r_{ij}))^2, \tag{5}$$

where $k_B T$ denotes the desired temperature in the unit of Boltzmann's constant k_B. In the original DPD model [4], the conservative force $\mathbf{F}_{ij}^{\mathrm{C}}$ is defined as

$$\mathbf{F}_{ij}^{\mathrm{C}} = a w^{\mathrm{C}}(r_{ij}) \hat{\mathbf{r}}_{ij}, \tag{6}$$

where a denotes the magnitude of the force, and the weight function $w^{\mathrm{C}}(r)$ vanishes when the inter-particle distance r is larger than a cutoff range r_{c}. The $\mathbf{F}_{ij}^{\mathrm{C}}$ is usually derived from a soft and unspecific weight function $w^{\mathrm{C}}(r_{ij})$, thus allowing for a fairly large integration time step. Different weight functions describe different material properties. A common choice for $w^{\mathrm{C}}(r_{ij})$ is

$$w^{\mathrm{C}}(r_{ij}) = 1 - r_{ij}/r_C \tag{7}$$

and

$$w^{\mathrm{R}} = w^{\mathrm{C}}. \tag{8}$$

The standard velocity Verlet algorithm can be used to integrate the resulting equations of motion in time [40]. [5] derived an empirical EOS for the original DPD method:

$$p = \rho k_B T + 0.1 a r_C^4 \rho^2, \tag{9}$$

where ρ is the average particle number density and p is the system pressure.

2.2. The many-body DPD model

However, the original DPD model is not sufficient to model multiphase fluid flow phenomena such as liquid-liquid interface and free capillary surface. A more complex EOS needs to be represented by DPD. To achieve that, [14] proposed a long-range attractive and short-range repulsive conservative force $\mathbf{F}^{\mathrm{C}}$:

$$\mathbf{F}_{ij}^{\mathrm{C}} = Aw^{\mathrm{C}}(r_{ij})\hat{\mathbf{r}}_{ij} + B(\bar{\rho}_i + \bar{\rho}_j)w_{\mathrm{d}}(r_{ij})\hat{\mathbf{r}}_{ij}, \tag{10}$$

which consists of a long-range attractive part $Aw^{\mathrm{C}}(r_{ij})\hat{\mathbf{r}}_{ij}$ that is density independent, and a short-range repulsive part $B(\bar{\rho}_i + \bar{\rho}_j)w_{\mathrm{d}}(r_{ij})\hat{\mathbf{r}}_{ij}$ that depends on a weighted average of the local particle density. The attractive component $Aw^{\mathrm{C}}(r_{ij})\hat{\mathbf{r}}_{ij}$ can be obtained by simply turning the sign of the original force parameter a (i.e., $A_{ij} < 0$, with a cutoff range $r_{\mathrm{c}} = 1$). The term $B(\bar{\rho}_i + \bar{\rho}_j)w_{\mathrm{d}}(r_{ij})\hat{\mathbf{r}}_{ij}$ is a many-body repulsive component with $B > 0$, and shorter cutoff in its weight function

$$w_d(r_{ij}) = 1 - r/r_d, \tag{11}$$

where $r_d < r_C$. The averaged local density, $\bar{\rho}_i$ at the position of particle i can be computed as $\bar{\rho}_i = \sum_{j \neq i} w_\rho(r_{ij})$, where the normalized weight function w_ρ needs to satisfy

$$\int_0^\infty 4\pi r^2 w_\rho(r)\, dr = 1. \tag{12}$$

For a three-dimensional computational domain, the w_ρ is defined as

$$w_\rho(r) = \frac{15}{2\pi r_d^3}(1 - r/r_d)^2. \tag{13}$$

Other forms of ω_ρ such as the Lucy kernel function were also used in literature [28]. The choice of ω_ρ formulation influences the determination of other model parameters

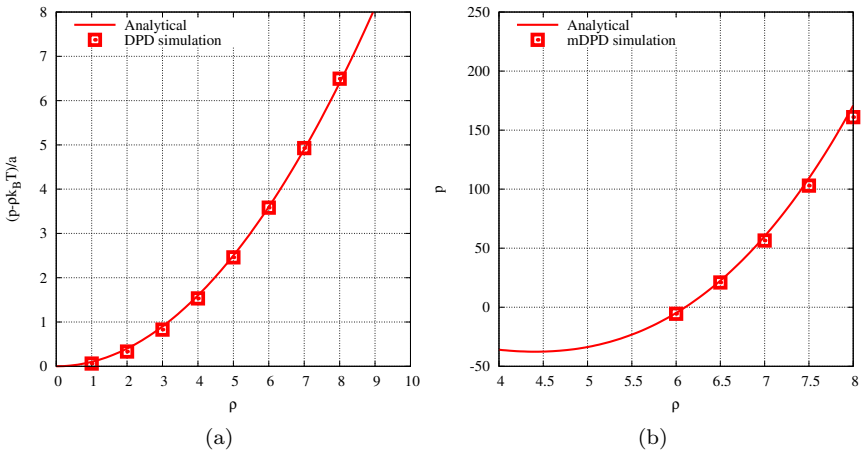

Figure 1. (a) Validation of the EOS for the original DPD model in Equation (9) with $k_BT = 1$, $\gamma = 4.5$, $r_C = 1$, and $a = 25$; (b) validation of the EOS for the mDPD model in Equation (14) with $k_BT = 1$, $\gamma = 4.5$, $r_C = 1$, $r_d = 0.75$, $A = -40$, $B = 25$, $\alpha = 0.101$, $c = 4.16$, and $d = 18$. Pressure for each particle's number density ρ is obtained by averaging over 1000 time steps after equilibrium, in a $10 \times 10 \times 10$ periodic box.

for fluid properties. The resulting model is widely called many-body DPD (mDPD) [9]. A fitted EOS for the mDPD model [14] is given below:

$$p = \rho k_B T + \alpha A \rho^2 + 2\alpha B r_d^4 (\rho^3 - c\rho^2 + d), \tag{14}$$

which includes the van der Waals loop. In Equation (14), A and B are the long-range attractive force parameter and short-range repulsive force parameter, respectively, in Equation (10); α, c and d are three independent fitting coefficients. A simple verification of EOS for the original DPD and mDPD models is shown in Figure 1.

3. Calibration and modification of the many-body DPD

3.1. Fluid static properties

In the original DPD model and many-body DPD model, fluid static properties such as the thermodynamic properties (i.e. the EOS in Equation (9) and Equation (14), respectively) and interfacial properties (i.e. free surface tension) depend only on the formulations of the conservative force. [41] verified that the influence of the dissipative and random forces on those fluid static properties is negligible, if a correct Boltzmann distribution is guaranteed by Equation (4) and Equation (5). To model the static

properties of a real fluid with mDPD, four parameters in the conservative force in Equation (10) will be calibrated, including the force coefficients A and B and cut-off radii r_C and r_d. Being a coarse-graining of MD, DPD systems are expected to predict bulk fluid properties of interest and thus allowed to neglect atomistic-scale details such as interactions and self-motion of fluid molecules. As far as liquid fluids in geological mesoporous confinement are concerned, the fluid pressure tend to vary across a wide range of pore sizes and thus mDPD is expected to accurately predict the fluid EOS. In the meantime, the fluid static properties in mesopores are strongly influenced by fluid-wall interactions. Accurate prediction of fluid free surface tension is a prerequisite for mDPD to qualify for free surface flow simulations in mesopores. Therefore, we choose the fluid EOS and free surface tension as two closures for the mDPD calibration of the conservative force parameters. Since the number of parameters to determine is larger than that of the closures, i.e. 4 versus 2, the calibration process is essentially to solve an under-determined system. This indicates multiple combinations of the parameters are possible in the solution space to satisfy the closures. We have found it practically possible to decrease the number of parameters needed for calibration with a fixed relation of $r_d = 0.75 r_C$, and retain only A, B and r_C as three independent parameters. Fixing $r_d = 0.75 r_C$ with $r_C = 1$ has been a common practice in literature [27–31]. We choose to keep this ratio in our model. However, using different r_d is also allowed for more complex models. It is worth noting that the fluid properties calculated in an mDPD system are very sensitive to all the cut-off radii.

An iterative calibration process for determining the mDPD conservative force parameters is concisely illustrated in Figure 2. The process consists of two major steps. For the first step, Equation (14) that describes the EOS for mDPD fluid is used to calibrate the A and B with the reference profile until a specified criterion of agreement is reached. The reference data can be taken from either available experimental measurements or molecular simulations. To begin with the calibration, we need to provide an initial guess for the three independent parameters, e.g. $A = -50$, $B = 25$ and $r_C = 1$ taken from [27]. Before calibrating A and B, we examined the values of the fitting coefficients α, c and d in Equation (14). We found that in order to well match the mDPD EOS profile with the system pressure calculated from mDPD simulations,

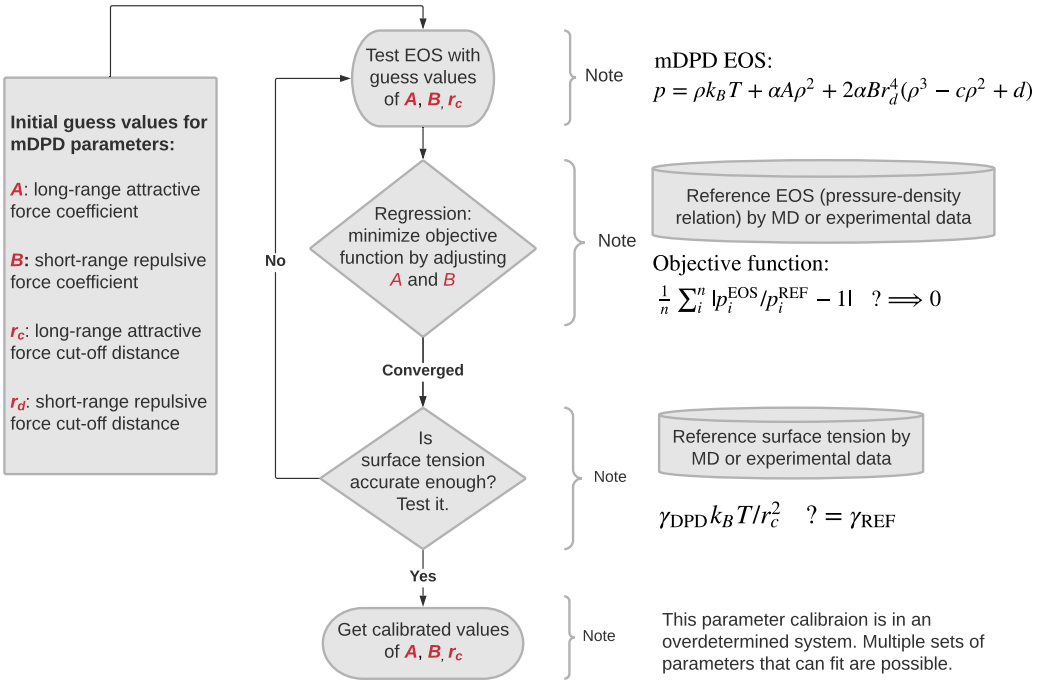

Figure 2. Schematic of a model parameter calibration process for mDPD.

the reference fitting coefficients need to be adjusted. For example, a combination of $\alpha = 0.101$, $c = 4.16$, $d = 19$ is found to work well for heptane, in which the values for α and c are identical to those in [14], whereas d is slightly modified. To determine A and B, we define an objective function as

$$f = \frac{1}{N}\sum_{n=1}^{N} |p_i^{\mathrm{EOS}}/p_i^{\mathrm{REF}} - 1|, \tag{15}$$

where p_i^{REF} is the i-th data point of reference pressure (with a total number of data points N), and p_i^{EOS} is the corresponding pressure calculated from the EOS with the same density as the i-th reference data point. By minimizing the objective function via a nonlinear regression algorithm, a pair of A and B values can be determined. In the meantime, we would like to note that a fully probabilistic model in a Bayesian framework [42–44] is in theory the best possible option for calibrating many model parameters, where both the values of model parameters and their estimate of uncertainty can be determined. However, the Bayesian is computationally much more expensive and would be more suitable for a complex model with many parameters to calibrate.

We would consider the Bayesian framework in future for more complex systems with many undetermined model parameters. In the current mDPD model designed to simulate flow of liquid hydrocarbon fluids, only a modest number of model parameters will need to be determined for predicting the fluid properties of interest. Therefore, we choose to use the presented iterative calibration process, which is relatively simple to implement and efficient for this specific problem. For the second step, an mDPD simulation with the A and B determined in the first step is performed to calculate the free surface tension of an unconfined bulk liquid and check against the reference data via conversion from the DPD reduced unit to the physical unit. If the simulated free surface tension does not match the reference value, r_C will be adjusted and then A and B will be re-calibrated in the first step. The two steps are repeated until the reference EOS and free surface tension are both matched by mDPD simulations.

3.2. Fluid dynamic properties

Given a fixed particle number density ρ in a DPD system, the fluid dynamic properties such as mass diffusivity D^* and kinematic viscosity ν^* (both in the DPD reduced unit) depend on the dissipative force and random force parameters, but are relatively irrelevant to the conservative force [5]:

$$D^* \approx \frac{45 k_B T}{2\pi\gamma\rho r_C^3} \tag{16}$$

$$\nu^* \approx \frac{45 k_B T}{4\pi\gamma\rho r_C^3} + \frac{2\pi\gamma\rho r_C^5}{1575} \tag{17}$$

where the conservative force cut-off distance r_C is used in [5] only because they assumed $w^{\mathrm{D}}(r_{ij}) = (w^{\mathrm{R}}(r_{ij}))^2 = (w^{\mathrm{C}}(r_{ij}))^2 = (1 - r_{ij}/r_C)^2$ for simplicity. In a general case, $w^{\mathrm{R}}(r_{ij})$ does not have to be equal to $w^{\mathrm{C}}(r_{ij})$. Note that Equation (16) and Equation (17) show the dependence of transport properties (diffusivity and viscosity) on DPD parameters, though the relationships are only approximate but not exact.

The correspondence of fluid dynamic properties between the DPD frame and

physical frame correlates to the correspondence of timescale between the two frames. The relation between the timestep in the DPD reduced unit, δt^*, and its counterpart in the physical unit, Δt, can be established based on either conversion from ν^* to its counterpart in the physical unit, ν [45]:

$$\Delta t_\nu = \delta t^* \frac{N_m \nu^* r_C^2}{\nu}, \tag{18}$$

or conversion from D^* to its counterpart in the physical unit, D [27]:

$$\Delta t_D = \delta t^* \frac{N_m D^* r_C^2}{D}, \tag{19}$$

where N_m is the DPD coarse-graining factor indicating the number of fluid molecules represented by one DPD bead. In a DPD system, adopting Equation (18) normally results in an inaccurate value of D, whereas adopting Equation (19) results in an inaccurate value of ν. For example, [5] reported that in the DPD modeling of water properties, the timescale derived via Equation (19) is about 1000 times greater than that via Equation (18). That is why it has been a long-standing challenging for a DPD fluid system to render the quantitatively correct viscosity and diffusivity simultaneously.

3.3. Modification of the mDPD model

To seek a possible solution for overcoming this challenge, we refer to the Schmidt number (Sc), a dimensionless number defined as the ratio of momentum diffusivity (kinematic viscosity) and mass diffusivity. The Schmidt number is used to characterize fluid flows in which there are simultaneous momentum and mass diffusion convection processes. Ideally, the Schmidt number is required to be identical between a DPD system and its corresponding physical system:

$$\mathrm{Sc} = \frac{\nu}{D} = \frac{\nu^*}{D^*}. \tag{20}$$

By substituting Equation (18) and Equation (19) into Equation (20), the above requirement translates to $\Delta t_D = \Delta t_\nu$. For a real fluid, ν and D are known based on either experimental measurement or molecular simulations. Therefore, in a DPD system with prescribed δt^*, N_m and r_C^2, a unique pair of ν^* and D^* must be found to satisfy the requirement of $\Delta t_D = \Delta t_\nu$. The search of the correct ν^* and D^* translates to the calibration of the parameters in Equation (16) and Equation (17), where the adjustable parameters include γ and r_C. Since the adjustment of r_C will alter the conservative force and subsequently the fluid static properties, we avoid doing so by introducing a new independent cut-off distance r_D to replace r_C in Equation (16) and Equation (17) and consequently decouple $w^{\mathrm{R}}(r_{ij})$ from $w^{\mathrm{C}}(r_{ij})$ in Equation (8). The introduction of r_D results in a number of updated formulations as follows:

$$w^{\mathrm{D}}(r) = (w^{\mathrm{R}}(r_{ij}))^2 = (1 - r_{ij}/r_D)^2, \tag{21}$$

$$D^* \approx \frac{45 k_B T}{2\pi\gamma\rho r_{\mathrm{D}}^3}, \tag{22}$$

$$\nu^* \approx \frac{45 k_B T}{4\pi\gamma\rho r_D^3} + \frac{2\pi\gamma\rho r_D^5}{1575}. \tag{23}$$

Incorporating the above modification into the mDPD model, γ and r_D can be adjusted to obtain the correct ν^* and D^* simultaneously, and subsequently reach the correct Schmidt number. As it can be inferred from the strong non-linearity of Equation (22) and Equation (23), there may be multiple possible combinations of γ and r_D to satisfy the unique pair of ν^* and D^*. To limit the search space for γ, we prescribe a test value range of γ between 4.5 and 18, which is typical in literature. For each test value of γ, a prescribed test value range of r_D value is examined. One solution combination of γ and r_D is obtained when the target values of ν^* and D^* are met simultaneously. This calibration process for ν^* and D^* is relatively trivial and thus is easily automated in this work.

3.4. Summary

In this section, we have presented a systematic approach for the mDPD model to calibrate and obtain the real fluid static properties of interest, including the liquid EOS and free surface tension. In the meantime, we have introduced an independent cut-off distance for the dissipative force in the mDPD model to make it much easier to obtain the real fluid dynamic properties of interest, including the fluid diffusivity and fluid viscosity. This is a novel and yet simplistic approach to overcome the long-standing challenge for a DPD fluid system to obtain the correct fluid diffusivity and viscosity simultaneously.

4. Numerical examples

In this section, we present numerical examples to demonstrate the accurate modeling of fluid properties for the liquids of interest. First, we will use heptane (an alkane with an intermediate chain length) as a representative hydrocarbon fluid for its abundance in subsurface hydrocarbon resources. The accurate and efficient mesoscale modeling of heptane with the modified mDPD model will serve as an important example for the development of mDPD models for other hydrocarbon fluids. Notice that we only consider the liquid phase of heptane in the pressure-temperature conditions relevant to the confinement in subsurface. To further demonstrate the robustness of the modified mDPD model, we revisit the benchmark problem of mesoscopic modeling of liquid water. Existing literature reported only a very limited portion of water properties with DPD. We will show that the modified mDPD model can provide an accurate prediction of water static and dynamic properties to a much broader extent. In this work, the MD simulations were carried out using LAMMPS [46] and the mDPD simulations were conducted using a package [21] based on LAMMPS.

4.1. Heptane

4.1.1. Problem setup

The reduced units are used for DPD systems. The first parameter to specify is the coarse-graining factor N_{m}. We choose N_{m} to be 1 for heptane, meaning that one DPD bead is used to represent the equivalent envelope volume of a heptane molecule, as shown in Figure 3. In general, N_{m} can be 2, 3, or larger for fluids. For example, $N_{\mathrm{m}} = 3$ is widely used for liquid water [27]. There is practically an upper limit of N_m to guarantee the numerical accuracy. When N_m exceeds a certain limit, the DPD beads will freeze into an ordered structure and cannot flow [47]. This work will study the heptane properties at two temperatures, 303K and 323K, respectively, for which the experimental measurements are available in literature.

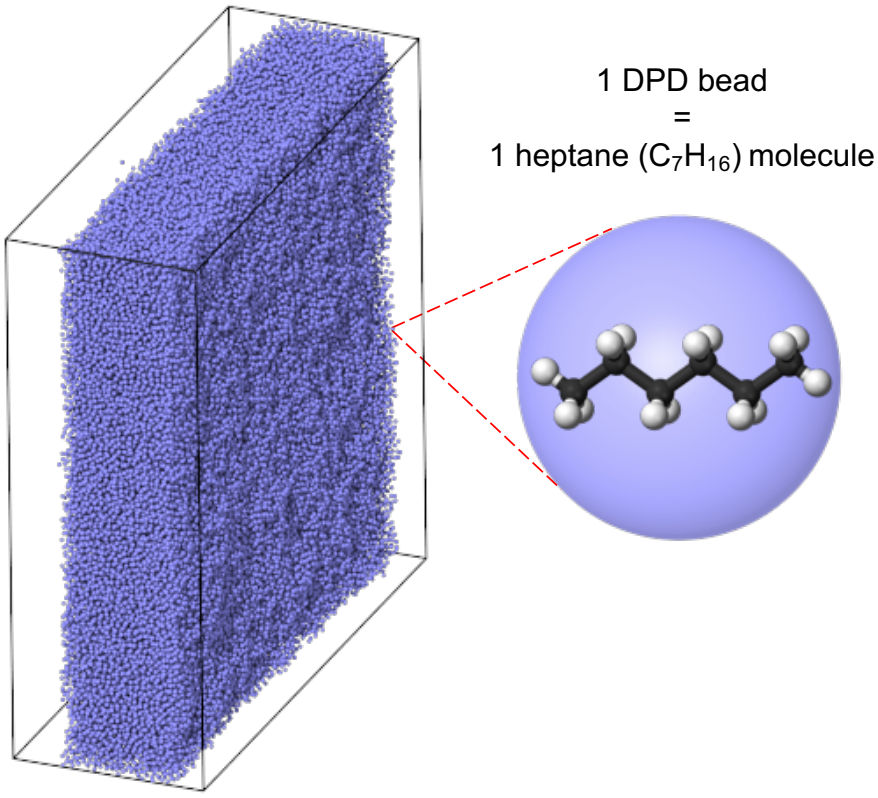

Figure 3. Simulation snapshot for the free surface of a bulk liquid modeled by the mDPD method. The bulk liquid comprises 150,000 mDPD particles.

To calibrate the mDPD model for the heptane EOS, we performed the simulations

with 5765 - 6400 mDPD beads in a periodic box with the lengths of sides, $L_x = L_y = L_z = 10$, in the reduced unit. The fluid compressibility will be guaranteed by the correct prediction of EOS. To provide numerical validation reference, we conducted the NVT MD simulations with 5765 - 6400 heptane molecules in a periodic box of $L_x = L_y = L_z = 112.4$ Å. The TraPPE-UA [48] and OPLS-UA force fields [49] were used for heptane molecules in the MD simulations. The size of the mDPD simulation box is equivalent to its MD counterpart in the SI units. The conversion from the DPD reduced units to the SI units will be discussed with more details in the following section. To calibrate the mDPD model for predicting the free surface tension of heptane, 150,000 mDPD beads were used in a periodic simulation box of $L_x = L_y = 50$ and $L_z = 20$, in the reduced unit, as shown in Figure 3. The surface tension can be calculated as follows:

$$\gamma = \int [p_{zz} - \frac{1}{2}(p_{xx} + p_{yy})]dz, \tag{24}$$

where p_{xx}, p_{yy} and p_{zz} are the diagonal components of the Cauchy stress tensor. The MD simulations were performed with a bulk of 96,000 heptane molecules to provide numerical reference of free surface tension.

To calibrate the mDPD model for predicting the fluid dynamic properties, we performed the simulation with a periodic box of $L_x = L_y = L_z = 10$ in the reduced unit. A total of 5765 and 5594 mDPD beads were used to in correspondence to the heptane densities at 303 K and 323 K, respectively. The dynamic viscosity μ can be calculated using the Green-Kubo relation:

$$\mu = \frac{V}{k_B T} \int_0^\infty < P_{\alpha\beta}(0) P_{\alpha\beta}(t) > dt, \tag{25}$$

where α and β are directions in the Cartesian coordinates (x,y,z), V is the volume of the system, and $P_{\alpha\beta}$ is the off-diagonal component ($\alpha \neq \beta$) in the pressure tensor. The mass diffusivity D is calculated using the Einstein relation:

$$\langle |r(t) - r(0)|^2 \rangle \ = 2dDt, \tag{26}$$

in which the term on the left stands for the mean-square displacement (MSD), $r(t)$ is the position of the bead at simulation time t, and $d = 3$ is the dimension of space. We would like to note that Equation (22) and Equation (23) are not used to calculate the fluid diffusivity and viscosity in the simulations, but to reflect the correlation between the fluid properties and the mDPD parameters.

4.1.2. Simulation results

Table 1 lists the parameters used in the DPD reduced units and their conversion in the physical units for liquid heptane at the ambient temperature of $T = 303$ K. In the table, r_c, ρ, p, γ, and κ^{-1} are the cut-off radius in conservative force term, number density, pressure, surface tension, and compressibility, respectively. $V = 246.3$ Å^3 is the envelope volume of a heptane molecule, $M = 100.2$ g $\cdot$ mol^{-1} is the molar weight of a heptane molecule, N_A is the Avogadro constant, k_B is the Boltzmann constant, n is the number of heptane molecules in the volume of 1 m^3. We would like to note that in DPD systems we normally set $r_c^* = 1$ (in the reduced unit) for convenience, though other values are also allowed. Once the value of r_c^* is fixed, it indicates that in Table 1 the formula that converts r_c^* to r_c (in the physical unit) and the formula that converts ρ^* (in the reduced unit) to ρ (in the physical unit) are equivalent. Nevertheless, We keep both formulae in Table 1 and also in the later tables for easy numerical validation. For $T = 303$ K, we used the experimentally-measured EOS [50] and surface tension

Table 1. Conversion of liquid heptane properties at 303 K from the DPD reduced units to the physical units.

DPD			Physical units	
Parameter	Value	DPD $\rightarrow$ physical units	Parameter	Value
Bead	1	N_m	1	1 heptane
r_c^*	1	$r_c^*(\rho^* N_m V)^{1/3}$	r_c	11.24 Å
ρ^*	5.765	$\rho^* N_m M / N_a r_c^3$	ρ	675.4 kg/m^3
p^*	0.034	$p^* k_B T / r_c^3$	p	1 bar
γ^*	5.9	$\gamma^* k_B T / r_c^2$	γ	19.49 mN m^{-1}
κ^{-1*}	55.8	$N_m / (n k_B T \kappa^{-1*})$	κ^{-1}	1.06×10^{-9} Pa^{-1}

[51] as the primary reference data in the conservative force parameter calibration. Applying the calibration process described in Section 3.1, we determined a set of the independent parameters: $A = -36$, $B = 25$, and $r_C = 11.24$ Å that satisfy the two

closures for $T = 303K$. When experimental results are not available, MD simulations can be performed to generate the reference data. In this study, the MD simulations were conducted to serve as additional reference for validation.

Figure 4 shows a comparison of the EOS (pressure-density profile) obtained by the experimental measurements, mDPD EOS, mDPD simulations and MD simulations, respectively. The pressure-density profile predicted by MD with the TraPPE-UA force field is about 20-25% lower than the experimental profile and the profile predicted by MD with the OPLS-UA force field is further lower. Because the two MD simulated profiles do not quite agree with each other and also because they do not match the experimental profile well, in this case we chose to calibrate the modified mDPD model parameters by fitting the experimental profile rather than the MD simulated profiles. Nevertheless, it is always possible to calibrate the modified mDPD model parameters by fitting the MD results and we recommend using MD results for the calibration when experimental data is not available. It is remarkable that the profile calculated by the mDPD EOS in Equation (14) and one obtained by the mDPD simulation agree well with each other and they both closely match the experimental data from the unconfined condition up to the confinement pressure of about 70 MPa. We would like to note that it is sufficient for the calibrated mDPD model to be able to predict an accurate EOS up to about 30 MPa, which corresponds to the upper limit of controlled pressure in an experimental mesoporous flow test. Above all, the calibrated mDPD model demonstrated the high fidelity for predicting the liquid heptane EOS. As a relevant note, it is worth mentioning that the difficulty to determine the model parameters can increase drastically for satisfying further higher fluid pressure (e.g. $>$ 90 MPa) while guaranteeing an accurate free surface tension.

Table 2 lists the free surface tensions and unconfined fluid densities obtained by the experimental measurement, mDPD simulation and MD simulation, respectively, at $T = 303$K. The surface tension calculated from the mDPD simulation agrees well with the experimental value. In comparison, the TraPPE-UA based MD simulation resulted in a slight over-prediction, whereas its OPLS-UA counterpart rendered a large over-prediction. Besides, the estimate errors in the MD simulations are one order of magnitude higher than that in the mDPD simulation. Moreover, a comparison between

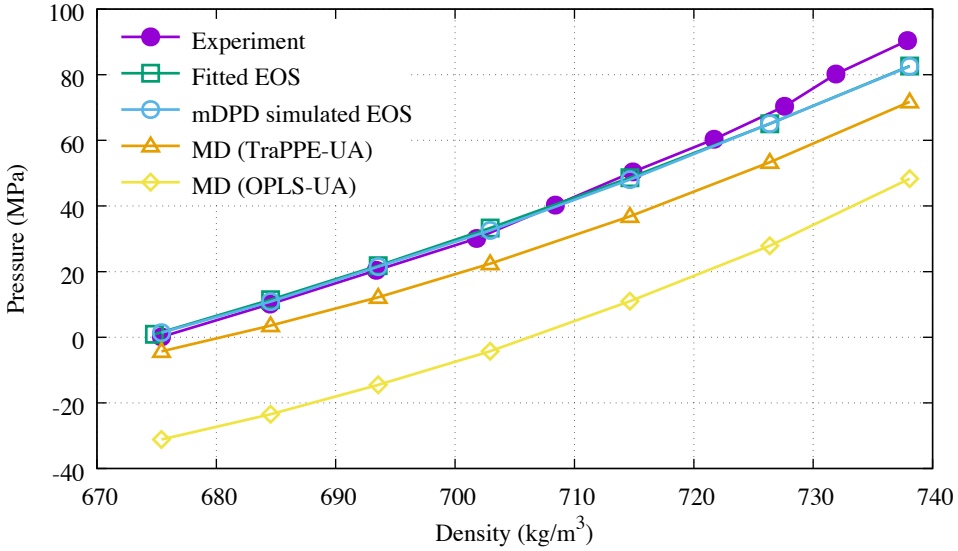

Figure 4. The heptane EOS at 303 K.

mDPD and MD on the time-averaged unconfined fluid density profiles across the bulk are shown in Figure 5. To obtain the density profile in the mDPD simulation, we set the bin size to be 0.1 and sampled the profile every timestep over a total of one million timesteps. The density profiles calculated by the mDPD and TraPPE-UA based MD simulations are close to each other and agree reasonably with the experimental value in Table 2, whereas the UPLS-UA based MD simulation shows a substantial over-prediction. It is also observed that the oscillations of fluid density in the vicinity of the free surface are negligible in the present mDPD simulation using the calibrated conservative force parameters for heptane, whereas the mDPD simulated water density profile showed remarkable oscillations [27]. The attractive force parameter A, which is -50 in the referred literature [27], is speculated as a main impact factor in the mDPD model for the oscillations in the vicinity of free surface. In addition, the bulk size of the fluid is another factor. Compared with the mDPD simulation of water that comprised of 1,000 - 10,000 beads in the referred literature [27], the present mDPD simulation of heptane used a much larger bulk size with 150,000 beads.

At $T = 303$ K, the measured liquid heptane dynamic viscosity ν is equal to 3.68×10^{-4} Pa·s [52] and the measured mass diffusivity D is equal to 3.22×10^{-9} $m^2 \cdot s^{-1}$ [53]. Together, they correspond to a Schmidt number of 169. To make our

Table 2. Heptane free surface tensions and unconfined densities obtained by experiments, mDPD and MD at 303K.

Method	γ (mN m^{-1})	ρ (kg m^{-3})
Experiment	19.49 [51]	675.4 [50]
mDPD	19.20 ± 0.13	674.0 ± 0.3
MD (TraPPE-UA)	18.58 ± 1.66	677.0 ± 1.4
MD (OPLS-UA)	25.19 ± 1.87	703.9 ± 1.4

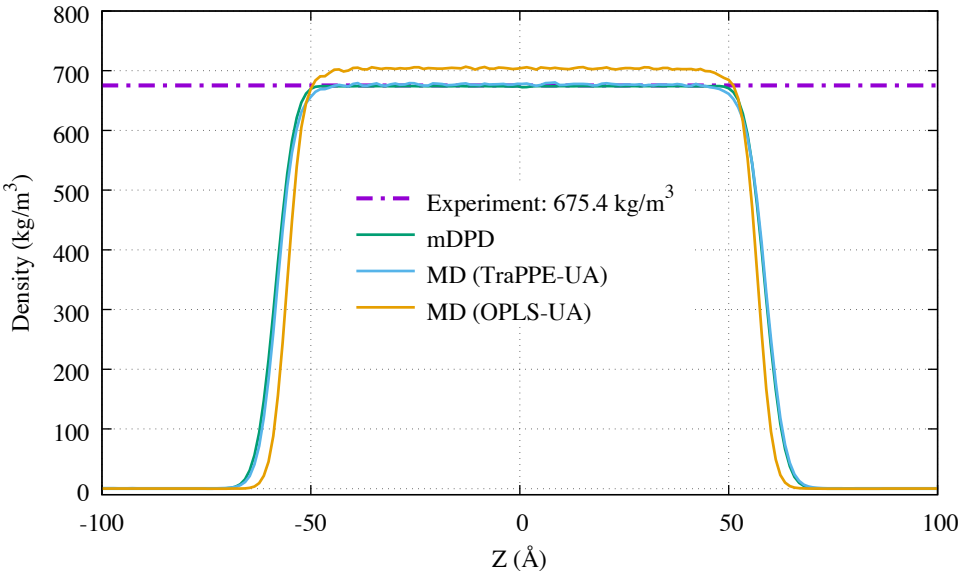

Figure 5. Unconfined density profiles of heptane as a function of bulk dimension at 303 K.

modified mDPD model accurately predict these dynamic properties simultaneously, we followed the procedure in Section 3.3 to calibrate the parameter γ and the new independent dissipative force cut-off radius r_D. Figure 6 shows a curve that represents the pairs of γ and r_D with which the mDPD model will generate a Schmidt number of 169. Along this curve, an optimal choice of γ and r_D will need to be determined. In general, increasing γ will result in the need for decreasing the timestep size to keep the simulation stable. On the other hand, increasing r_D will result in the increase of computational costs, as the pairs of mDPD beads in the dissipative and random forces calculations will increase. Since r_D increases sharply when γ is below 8, a practical choice of the pair of γ and r_D should be in the range of $r_D < 2$ and $\gamma < 18$ for a reasonable timestep size and computational costs. We would like to note that the choice of γ and r_D along the curve in Figure 6 does not affect the EOS and free

surface tension calibrated by the conservative force parameters. Above all, our rigorous evaluation proves an excellent fidelity of the modified mDPD model for capturing the important fluid static properties and dynamic properties of heptane simultaneously at the ambient temperature.

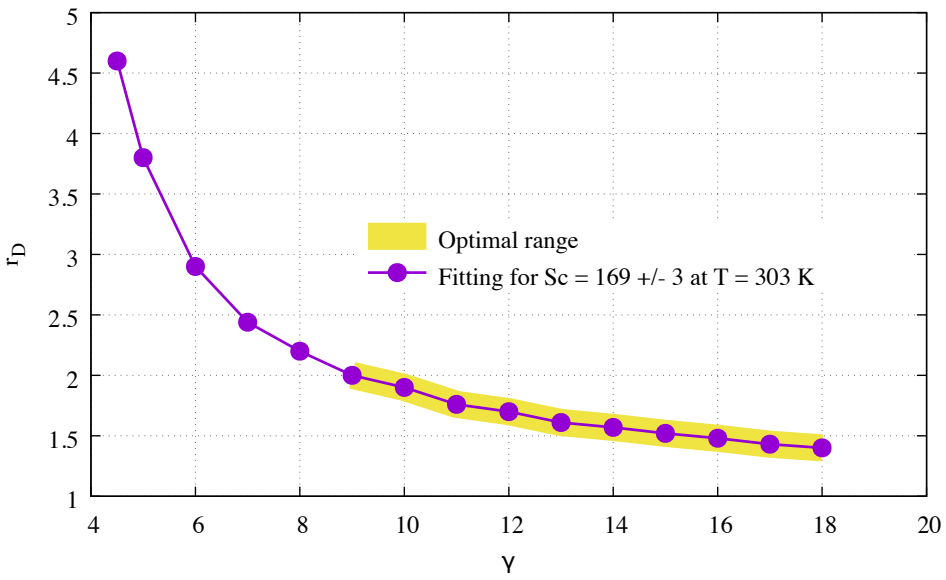

Figure 6. The calibrated dissipative force parameters γ and r_D for the correct Schmidt number of heptane at 303 K.

To demonstrate the robustness of the modified mDPD method and our calibration approach, we present another example of heptane at $T = 323$K, as the experimental measurements of the fluid properties are available for reference. Table 3 lists the parameters used in the DPD reduced units and their conversion in the physical units for liquid heptane at $T = 323$ K. The envelope volume V for one heptane molecule is 252.5 Å^3, which is slightly larger than $T = 303$ K due to thermal expansion. Following the calibration process in Section 3.1, we determined a set of the independent parameters in the conservative force: $A = -34$, $B = 25$ and $r_C = 11.22$ Å to satisfy the two closures for $T = 323$K. We also conducted MD simulations to serve as additional reference for validation.

Figure 7 displays a comparison of the 323 K liquid heptane EOS obtained by the experimental data, calculations with the mDPD EOS, mDPD simulations and MD simulations, respectively. The EOS predicted by the mDPD simulations and mDPD EOS closely match each other and they agree well with the experimental data [50]. The

Table 3. Conversion of liquid heptane properties at 323 K from the DPD reduced units to the physical units.

DPD			Physical units	
Parameter	Value	mDPD $\rightarrow$ physical units	Parameter	Value
Bead	1	N_m	1	1 heptane
r_c^*	1	$r_c^*(\rho^* N_m V)^{1/3}$	r_c	11.22 Å
ρ^*	5.594	$\rho^* N_m M/N_a r_c^3$	ρ	658.9 kg/m^3
p^*	0.032	$p^* k_B T/r_c^3$	p	1 bar
γ^*	4.9	$\gamma^* k_B T/r_c^2$	γ	17.44 mN m^{-1}
κ^{-1*}	48.0	$N_m/(n k_B T \kappa^{-1*})$	κ^{-1}	1.18×10^{-9} Pa^{-1}

EOS predicted by the MD simulation results based on the TraPPE-UA and OPLS-UA force potentials agree with each, but they show an under-prediction of the fluid pressure by about 10 MPa throughout the tested range of confined density. Table 4 lists the 323 K free surface tensions and unconfined density of bulk heptane obtained by the experiments, mDPD simulations and MD simulations, respectively. The free surface tension calculated from the mDPD simulation agrees well with the experimental value. In comparison, the TraPPE-UA based MD simulation resulted in a slight under-prediction, whereas its OPLS-UA counterpart rendered a large over-prediction. Besides, the estimate errors in the MD simulations are one order of magnitude higher than that in the mDPD simulation. Further, a comparison between mDPD and MD simulation results on the time-averaged unconfined heptane density profiles across the bulk are shown in Figure 8. To obtain the density profile in the mDPD simulation, we specified the bin size to be 0.1 and sampled the profile every time step over a total of one million time steps, which were the same with the setup in the case of $T = 303$K. Again, the mDPD model provided an accurate prediction of the surface tension and unconfined fluid density with low estimate errors, whereas the two MD models rendered either slight over-prediction or under-prediction of those properties with much higher estimate errors.

At $T = 323$ K, the measured liquid heptane dynamic viscosity ν is equal to 3.03×10^{-4} Pa·s [52] and the measured mass diffusivity D is equal to 4.47×10^{-9} m^2·s^{-1} [54]. Compared with the values of those properties at $T = 303K$, the dynamic viscosity is slightly lower whereas the mass diffusivity is larger. Together, they correspond to a Schmidt number of 103. To make our modified mDPD model accurately predict

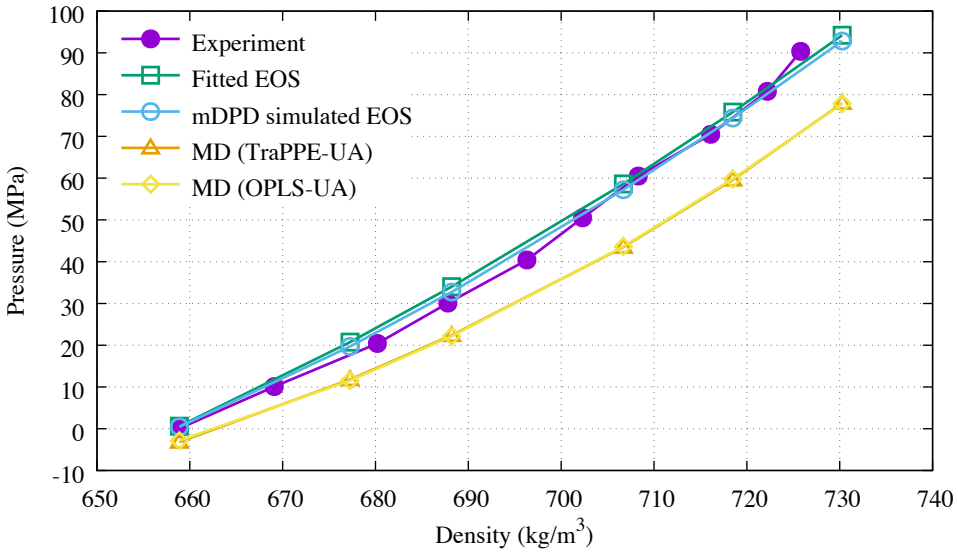

Figure 7. The fluid EOS for bulk heptane at 323 K.

Table 4. Heptane free surface tensions and unconfined densities obtained by experiments, mDPD and MD at 323K.

Method	γ (mN m^{-1})	ρ (kg m^{-3})
Experiment	17.44 [51]	658.9 [50]
mDPD	17.73 ± 0.14	658.6 ± 0.1
MD (TraPPE-UA)	16.62 ± 1.64	659.0 ± 1.1
MD (OPLS-UA)	22.97 ± 1.61	688.6 ± 1.3

these dynamic properties simultaneously, we followed the procedure in Section 3.3 to calibrate the parameter γ and the new independent dissipative force cut-off radius r_D. Figure 9 shows a curve that represents the pairs of γ and r_D with which the mDPD model will generate a Schmidt number of 103. Since r_D increases sharply when γ is below 7, a practical choice of the pair of γ and r_D should be in the range of $r_D < 2$ and $\gamma < 18$ to guarantee reasonable computational costs. The choice of γ and r_D along the curve in Figure 9 does not affect the EOS and free surface tension calibrated by the conservative force parameters. Above all, the study of liquid heptane at $T = 323$ has demonstrated the robustness and accuracy of the modified mDPD model for predicting the important fluid static properties and dynamic properties of heptane simultaneously at an elevated temperature.

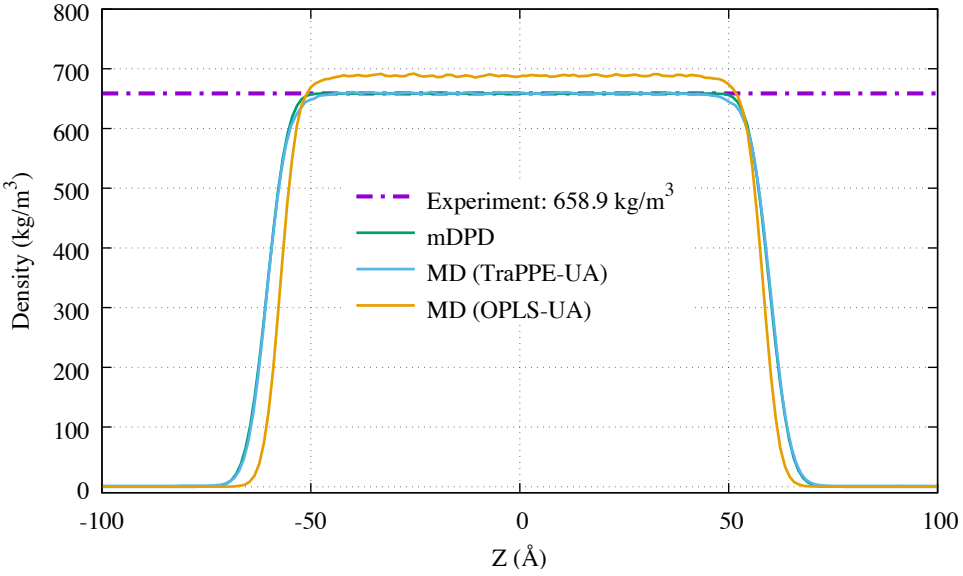

Figure 8. Unconfined density profiles of heptane as a function of bulk dimension at 323 K.

4.1.3. Sensitivity of bulk size in MD

As a side effort, we investigated the influence of bulk size on the free surface tension calculation in MD simulations. At each of the two tested temperatures (303 K and 323 K) and for each of the two force field models (TraPPE-UA and OPLS-UA), three simulations were conducted with the the bulk size successively quadrupled by doubling the extension of the two directions in the plane normal to the free surface, respectively, as shown in Table 5. Test results show that the increase of bulk size had little influence on the time-averaged values of the free surface tension. This also indicates the limited accuracy of the two MD force field models to capture the experimentally measured free surface tension values of heptane. However, it is remarkable to see that their estimate errors in the predicted values decrease with the increase of the bulk sizes.

4.1.4. Efficiency of mDPD

To demonstrate the efficiency of mDPD, we performed a comparative timing test for mDPD and MD simulations in a series of equivalent unconfined bulk volumes of liquid heptane at $T = 303$ K. All the simulations were conducted on a laptop using one CPU core (2.6 GHz Intel Core i7) for timing. We define the speedup of mDPD over MD as the ratio of mDPD simulation wall time and MD simulation wall time for completing

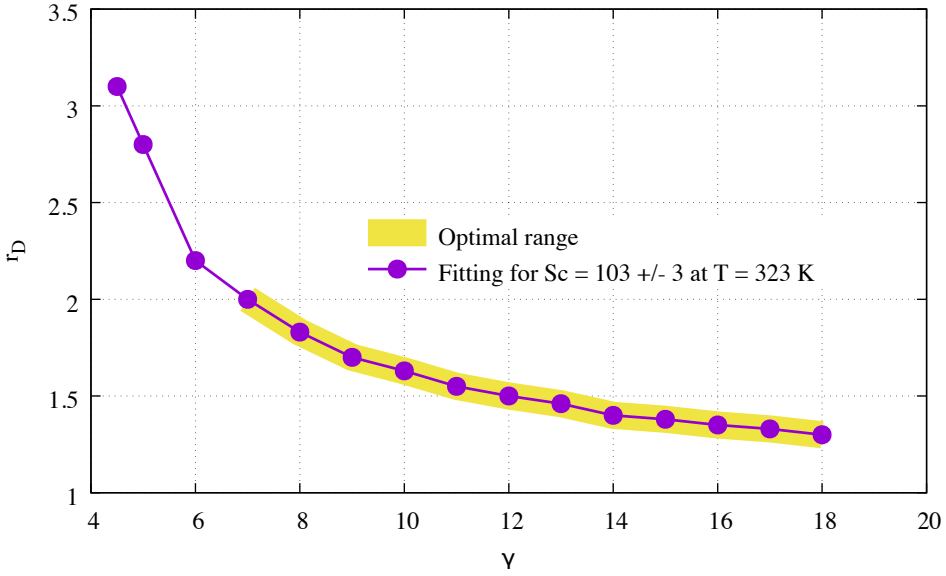

Figure 9. The calibrated dissipative force parameters γ and r_D for the correct Schmidt number of heptane at 323 K.

Table 5. Heptane free surface tensions calculated in MD simulations with different bulk sizes at 303K and 323 K.

T (K)	Molecules	γ (mN m^{-1}) (TraPPE-UA)	γ (mN m^{-1}) (OPLS-UA)
303	6000	18.57 ± 6.54	25.24 ± 7.16
303	24000	18.98 ± 3.15	25.16 ± 3.49
303	96000	18.58 ± 1.66	25.19 ± 1.87
323	6000	16.58 ± 6.87	22.88 ± 6.76
323	24000	16.72 ± 3.15	22.75 ± 3.33
323	96000	16.62 ± 1.64	22.97 ± 1.61

a specified physical time duration. The mDPD dissipative force parameters are chosen as $\gamma = 12.5$ and $r_D = 1.65$, resulting in an mDPD timestep that is equivalent to 6.84 ps in the physical unit. The timing results are shown in Figure 10, exhibiting a speedup between 430x and 510x for the heptane bulk volume ranging from about one thousand nm^3 to nearly one million nm^3.

4.2. Water

In this section we revisit the benchmark problem of mesoscopic modeling of water at 298 K to demonstrate the broad applicability of the modified mDPD model. Water is used as a common benchmark fluid for the instrumented test of pressure-driven

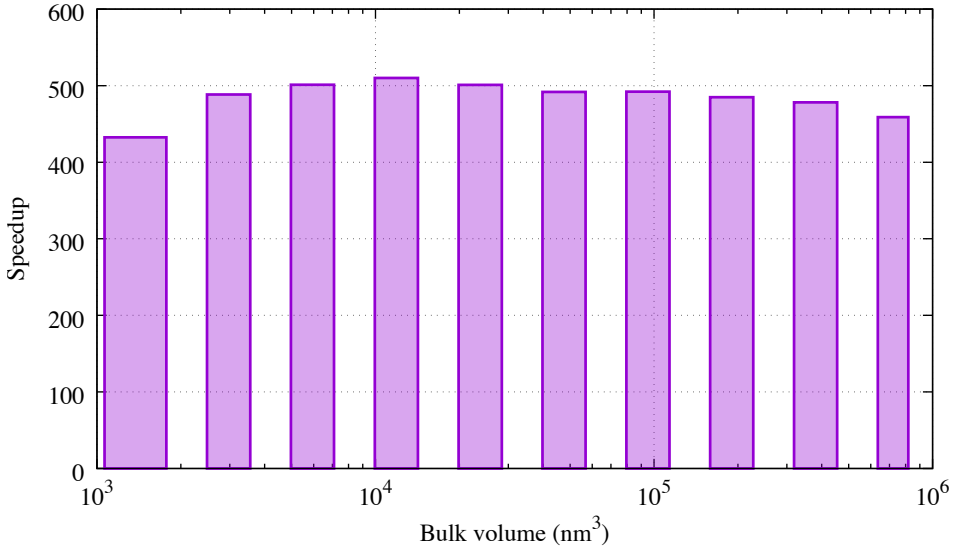

Figure 10. Speedup of mDPD over MD in equivalent simulation system volumes for liquid heptane at 303 K.

flow in nano- to micro-porous materials and thus it is of high interest for modelers to apply a high-fidelity DPD model for the corresponding water flow simulations. All of the previous DPD works attempted to capture only a certain part of liquid water properties and none of them reported a DPD model and the associated parameter space that can capture a wider extent of the water properties of interest, including the EOS in a range of practical interest (i.e. from the ambient pressure to the injection pressure that spans 20 - 50 MPa), free surface tension, diffusivity, and viscosity. Most of the previous DPD works used a coarse-graining factor of $N_m = 3$ for water [19,27,31,55]. However, this work uses $N_m = 4$ for water with the reason to be discussed later. Following the static fluid property calibration process in Section 3.1, we determined a set of the independent parameters in the mDPD conservative force: $A = -44.6$ and $B = 14$ with $r_C = 10.2$ Å ($r_C^* = 1$) for water at $T = 298$ K. Table 6 lists the parameters used in the DPD reduced units and their conversion in the physical units. The envelope volume for one water molecule, V, is 30 Å^3. The molar weight of one water molecule is $M = 18$ g $\cdot$ mol^{-1}.

Figure 11 displays the EOS of water at 298 K obtained by the experimental measurements [56], mDPD EOS based calculations, and mDPD simulations. The profiles predicted by our mDPD simulations and mDPD EOS closely match each other and

Table 6. Conversion of liquid water properties at 298 K from the DPD reduced units to the physical units.

DPD			Physical units	
Parameter	Value	mDPD $\rightarrow$ physical units	Parameter	Value
Bead	1	N_m	4	4 water
r_c^*	1	$r_c^*(\rho^* N_m V)^{1/3}$	r_c	10.2 Å
ρ^*	8.844	$\rho^* N_m M/N_a r_c^3$	ρ	997.05 kg/m^3
p^*	0.0258	$p^* k_B T/r_c^3$	p	1 bar
γ^*	18.2	$\gamma^* k_B T/r_c^2$	γ	71.99 mN m^{-1}
κ^{-1*}	65.48	$N_m/(n k_B T \kappa^{-1*})$	κ^{-1}	4.5×10^{-10} Pa^{-1}

they agree well with the experimental data [56] from the ambient pressure up to 80 MPa, which encloses the pressure range of experimental and engineering interest. For comparison, we also carried out the mDPD EOS calculations and mDPD simulation using the parameters ($A = -50.8$ and $B = 25$ with $N_m = 3$) slightly adjusted based on [27], as shown in Figure 11. Our test indicates that the parameters reported in their work ($A = -50$ and $B = 25$ with $N_m = 3$) may have only guaranteed the correct free surface tension, whereas the simulated EOS deviates significantly from the experimental data. Using the calibration approach of this work, we have found that a slight modification of the parameter A from -50 to -50.8 can remarkably improve the accuracy of the EOS in the lower pressure range. However, the deviation of the profile is still large in the higher pressure range and cannot be further reduced with any stable combinations of the mDPD conservative force parameters, which indicates the limitation of $N_\mathrm{m} = 3$ to produce an accurate EOS and free surface tension simultaneously. That is why we tested other values of N_m and finally found $N_\mathrm{m} = 4$ to be a much more robust choice that can satisfy our requirement. The free surface tension of water predicted by our mDPD simulation is 71.44 ± 0.19 mN m^{-1}, which agrees well with the experimental data (71.99 mN m^{-1}) [57].

The dynamic viscosity of water at 298 K is 8.92×10^{-4} Pa·s [58] and the diffusivity of water at 298 K is 2.23×10^{-9} m^2 s^{-1} [59]. Together, they correspond to a Schmidt number of 401. There is a possible ambiguity about understanding the diffusivity of DPD fluids, if one DPD bead is configured to represent the equivalent mass of multiple fluid molecules, for example, four water molecules in the present case. We would like to restate that DPD is a mesoscopic hydrodynamics model for bulk fluids and their

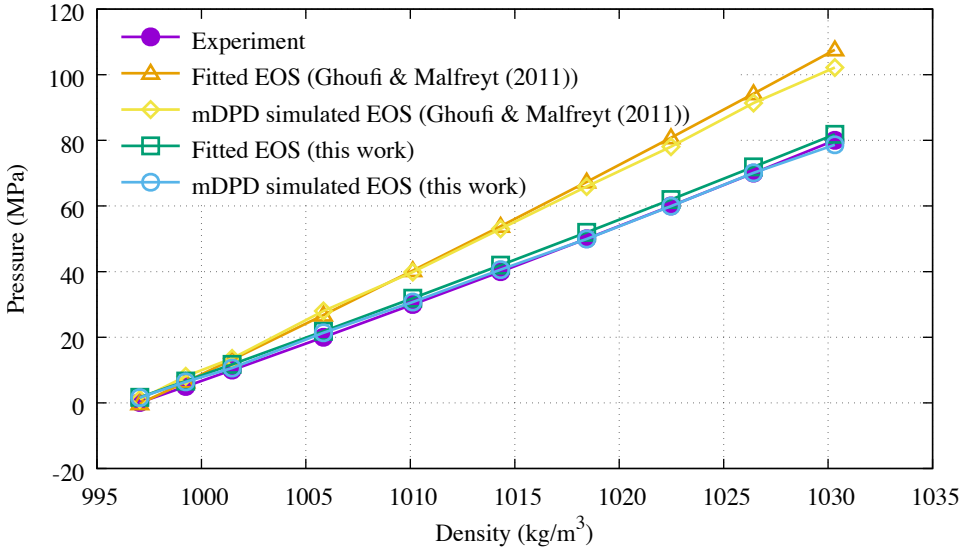

Figure 11. The fluid EOS for bulk water at 298 K. The reference numerical results used the parameters as $A = -50.8$, $B = 25$ with $N_m = 3$, which were slightly modified from [27]. The present work used $A = -44.6$ and $B = 14$ with $N_m = 4$ as a result of rigorous calibration.

properties; it is not valid to compare one DPD bead and its diffusivity to a cluster of fluid molecules and their diffusivity in an isolated context. Therefore, it is legitimate to compare the liquid water diffusivity predicted by the modified mDPD model to the experimental measurement. Above all, using the calibration approach in Section 3.2, we determined the combinations of γ and r_D with which the modified mDPD model can predict the accurate Schmidt number of water at 298 K, as shown in Figure 12. The choice of γ and r_D along the curve in Figure 12 does not affect the EOS and free surface tension already calibrated by the conservative force parameters. Similar to the cases of heptane discussed in Section 4.1.2, a practical choice of the pair of γ and r_D should be bounded by $r_D < 2$ and $\gamma < 18$ to guarantee the reasonable computational costs. Above all, the ability and robustness of the modified mDPD model to accurately predict the water and hydrocarbon static and dynamic properties, and EOS in a large range of confinement pressure make the model attractive for applications in simulations of instrumented pressure-drive flow test in meso-confinement.

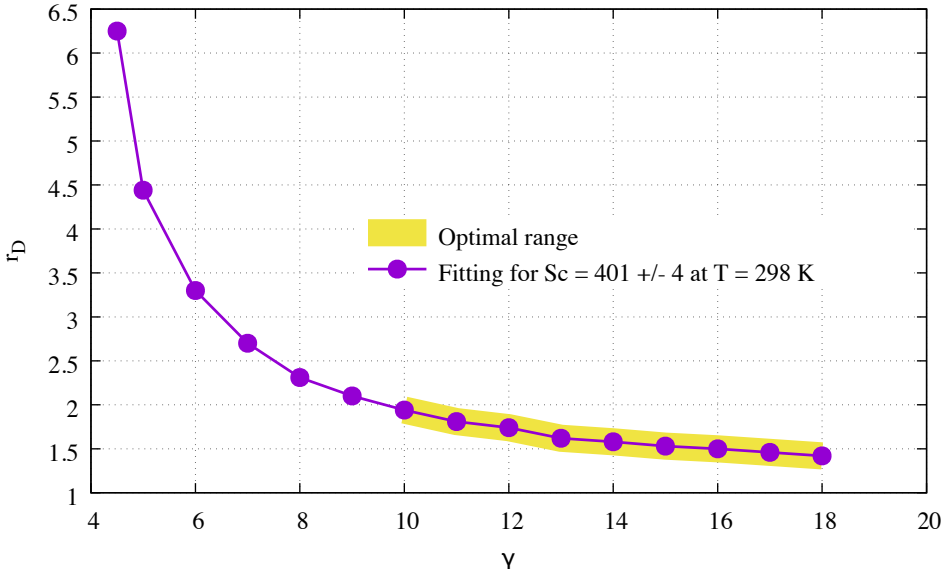

Figure 12. The calibrated dissipative force parameters γ and r_D for the correct Schmidt number of water at 298 K.

5. Conclusions

In summary, we conclude the major contributions and scientific advancement of this work as follows. We have developed a modified many-body DPD (mDPD) model by introducing a new independent degree of freedom in the model (dissipative force cut-off radius decoupled from the conservative force cut-off radius). The modified mDPD model can accurately predict the real-fluid bulk EOS subjected to large changes of pressure (from the ambient pressure to 80-90 MPa), free surface tension, diffusivity and viscosity, and thus has overcome a primary challenge of the original mDPD model (and also all other multiphase-enabled DPD models) to predict the static and dynamic properties of real liquid fluids simultaneously. Another major contribution of this work is that a rigorous calibration approach that uses reference data, including experimental and/or MD simulation results, has been introduced to parameterize the modified mDPD for real fluids. For the first time a DPD model among all the multiphase-enabled DPD methods has been made practically usable for simulating real liquid fluids with accurate static and dynamic properties at the same time. We have presented a series of numerical examples to demonstrate the predictability of properties of real liquid fluids by simulating bulk heptane. Heptane was used as a representative

liquid hydrocarbon for its abundance in source rocks. The new methodology can be applied to other hydrocarbons as well, as they have similar properties with differences in the ranges of values. Our timing test has shown that the modified mDPD model is over two orders of magnitude faster than its MD counterpart for simulations of bulk heptane in equivalent volumes, indicating the suitability of the model for accurate and efficient simulations of fluid transport in the mesoscale.

The robustness and versatility of our modified mDPD method as well as the calibration approach are further demonstrated by application of the methodology to model liquid water. Notice that the properties of liquid water are drastically different from hydrocarbons. This is the first time that a DPD model is reported to provide an accurate prediction of water static and dynamic properties simultaneously and to a much broader extent of pressure changes. All the previous DPD works in the literature showed only a very limited portion of the water properties (either static or dynamic) and only under the ambient pressure. Table 7 provides a summary of the calibrated model parameters for liquid heptane and water, respectively. We would like to note that in general there is no unique combination of γ and r_D to achieve the correct fluid dynamic properties for each set of fluid and temperature, as shown in Figure 6, Figure 9 and Figure 11. Nevertheless, we recommend a combination of γ and r_D for each in Table 7 as reference for future applications.

Above all, the modified mDPD model developed in this work for simulating real fluid properties is a prerequisite for our follow-on model application of liquid hydrocarbon flow in mesoporous confinement. This also indicates the need for calibration of real fluid-solid interactions [60–62] following a similar approach of this work to accurately account for the capillary flow [39] and slip flow [63].

Table 7. A summary of the calibrated mDPD model parameters (in reduced unit) for liquid heptane at 303 K and 323 K and water at 298 K, respectively.

Fluid	T (K)	N_m	A	B	r_c	r_d	γ	r_D
heptane	303	1	-36	25	1	0.75	12	1.7
heptane	323	1	-34	25	1	0.75	12	1.5
water	298	4	-44.6	14	1	0.75	12	1.74

Acknowledgement

The research [1] is primarily supported by EFRC-MUSE, an Energy Frontier Research Center funded by the U.S. Department of Energy, Office of Science, Basic Energy Sciences under Award No. DE-SC0019285. The software development in this work is supported through the Idaho National Laboratory (INL) Laboratory Directed Research & Development (LDRD) Program under the U.S. Department of Energy Idaho Operations Office Contract DE-AC07-05ID14517. The research used resources in the High Performance Computing Center at INL, which is supported by the Office of Nuclear Energy of the U.S. Department of Energy and the Nuclear Science User Facilities under Contract No. DE-AC07-05ID14517.

References

[1] Collell J, Galliero G, Vermorel R, et al. Transport of multicomponent hydrocarbon mixtures in shale organic matter by molecular simulations. The Journal of Physical Chemistry C. 2015;119(39):22587–22595.

[2] Huang H, Meakin P, Liu M. Computer simulation of two-phase immiscible fluid motion in unsaturated complex fractures using a volume of fluid method. Water Resources Research. 2005;41(12).

[3] Huang H, Meakin P, Liu M, et al. Modeling of multiphase fluid motion in fracture intersections and fracture networks. Geophysical Research Letters. 2005;32(19).

[4] Hoogerbrugge PJ, Koelman JMVA. Simulating Microscopic Hydrodynamic Phenomena with Dissipative Particle Dynamics. EPL (Europhysics Letters). 1992;19(3):155.

[5] Groot RD, Warren PB. Dissipative particle dynamics: Bridging the gap between atomistic and mesoscopic simulation. The Journal of Chemical Physics. 1997;107(11):4423–4435.

[6] Marsh C. Theoretical Aspects of Dissipative Particle Dynamics [dissertation]. University of Oxford; 1998.

[7] Moeendarbary E, Ng TY, Zangeneh M. Dissipative particle dynamics: introduction, methodology and complex fluid applications – a review. International Journal of Applied Mechanics. 2009;1(04):737–763.

[8] Liu MB, Liu GR, Zhou LW, et al. Dissipative particle dynamics (DPD): an overview and

[1] Approved for public release (INL/JOU-20-57228)

recent developments. Archives of Computational Methods in Engineering. 2015;22(4):529–556.

[9] Li Z, Bian X, Li X, et al. Dissipative particle dynamics: foundation, evolution, implementation, and applications. In: Particles in flows. Springer; 2017. p. 255–326.

[10] Pan W. Single Particle DPD: Algorithms and Applications [dissertation]. Brown University; 2010.

[11] Pan W, Fedosov DA, Caswell B, et al. Predicting dynamics and rheology of blood flow: A comparative study of multiscale and low-dimensional models of red blood cells. Microvascular Research. 2011;82(2):163–170.

[12] Tang Y, Karniadakis G. Accelerating dissipative particle dynamics simulations on GPUs: Algorithms, numerics and applications. Computer Physics Communications. 2014; 185(11):2809–2822.

[13] Blumers AL, Tang YH, Li Z, et al. GPU-accelerated red blood cells simulations with transport dissipative particle dynamics. Computer Physics Communications. 2017;217:171–179.

[14] Warren PB. Vapor-liquid coexistence in many-body dissipative particle dynamics. Physical Review E. 2003;68(6):066702.

[15] Tiwari A, Abraham J. Dissipative-particle-dynamics model for two-phase flows. Physical Review E. 2006;74(5):056701.

[16] Heldele R, Schulz M, Kauzlaric D, et al. Micro powder injection molding: process characterization and modeling. Microsystem Technologies. 2006;12(10-11):941–946.

[17] Visser DC, Hoefsloot HCJ, Iedema PD. Modelling multi-viscosity systems with dissipative particle dynamics. Journal of Computational Physics. 2006;214(2):491–504.

[18] Liu M, Meakin P, Huang H. Dissipative particle dynamics with attractive and repulsive particle-particle interactions. Physics of Fluids. 2006;18(1):017101.

[19] Liu M, Meakin P, Huang H. Dissipative particle dynamics simulation of fluid motion through an unsaturated fracture and fracture junction. Journal of Computational Physics. 2007;222(1):110–130.

[20] Liu M, Meakin P, Huang H. Dissipative particle dynamics simulation of pore-scale multiphase fluid flow. Water Resources Research. 2007;43:W04411.

[21] Xia Y, Goral J, Huang H, et al. Many-body dissipative particle dynamics modeling of fluid flow in fine-grained nanoporous shales. Physics of Fluids. 2017;29(5):056601.

[22] Xia Y, Blumers A, Li Z, et al. A GPU-accelerated package for simulation of flow in nanoporous source rocks with many-body dissipative particle dynamics. Computer

Physics Communications. 2020;247:106874.

[23] Pagonabarraga I, Frenkel D. Dissipative particle dynamics for interacting systems. The Journal of Chemical Physics. 2001;115(11):5015–5026.

[24] Trofimov SY, Nies ELF, Michels MAJ. Thermodynamic consistency in dissipative particle dynamics simulations of strongly nonideal liquids and liquid mixtures. The Journal of Chemical Physics. 2002;117(20):9383–9394.

[25] Trofimov SY, Nies ELF, Michels MAJ. Constant-pressure simulations with dissipative particle dynamics. The Journal of Chemical Physics. 2005;123(14):144102.

[26] Vanya P, Crout P, Sharman J, et al. Liquid-phase parametrization and solidification in many-body dissipative particle dynamics. Physical Review E. 2018;98(3):033310.

[27] Ghoufi A, Malfreyt P. Mesoscale modeling of the water liquid-vapor interface: A surface tension calculation. Physical Review E. 2011;83(5):051601.

[28] Li Z, Hu GH, Wang ZL, et al. Three dimensional flow structures in a moving droplet on substrate: A dissipative particle dynamics study. Physics of Fluids. 2013;25(7):072103.

[29] Chen C, Zhuang L, Li X, et al. A many-body dissipative particle dynamics study of forced water–oil displacement in capillary. Langmuir. 2011;28(2):1330–1336.

[30] Chen C, Lu K, Zhuang L, et al. Effective fluid front of the moving meniscus in capillary. Langmuir. 2013;29(10):3269–3273.

[31] Chen C, Lu K, Li X, et al. A many-body dissipative particle dynamics study of fluid–fluid spontaneous capillary displacement. RSC Advances. 2014;4(13):6545–6555.

[32] Espanol P. Dissipative Particle Dynamics with Energy Conservation. EPL (Europhysics Letters). 1997;40(6):631.

[33] Li Z, Tang YH, Lei H, et al. Energy-conserving dissipative particle dynamics with temperature-dependent properties. Journal of Computational Physics. 2014;265:113–127.

[34] Ripoll M, Espanol P, Ernst MH. Dissipative Particle Dynamics with Energy Conservation: Heat Conduction. International Journal of Modern Physics C. 1998;9(08):1329–1338.

[35] Avalos JB, Mackie AD. Dynamic and transport properties of dissipative particle dynamics with energy conservation. The Journal of Chemical Physics. 1999;111(11):5267–5276.

[36] Zhang K, Li J, S C, et al. Temperature-dependent properties of liquid-vapour coexistence system with many-body dissipative particle dynamics with energy conservation [Arxiv:2007.09899]; 2020.

[37] Groot RD, Rabone KL. Mesoscopic simulation of cell membrane damage, morphology change and rupture by nonionic surfactants. Biophysical journal. 2001;81(2):725–736.

[38] Khedr A, Striolo A. Dpd parameters estimation for simultaneously simulating water–oil interfaces and aqueous nonionic surfactants. Journal of chemical theory and computation. 2018;14(12):6460–6471.

[39] Arienti M, Pan W, Li X, et al. Many-body dissipative particle dynamics simulation of liquid/vapor and liquid/solid interactions. The Journal of Chemical Physics. 2011; 134(20):204114.

[40] Revenga M, Zuniga I, Espanol P. Boundary conditions in dissipative particle dynamics. Computer Physics Communications. 1999;121:309–311.

[41] Goicochea AG, Altamirano MAB, Hernández JD, et al. The role of the dissipative and random forces in the calculation of the pressure of simple fluids with dissipative particle dynamics. Computer Physics Communications. 2015;188:76–81.

[42] Angelikopoulos P, Papadimitriou C, Koumoutsakos P. Bayesian uncertainty quantification and propagation in molecular dynamics simulations: a high performance computing framework. The Journal of chemical physics. 2012;137(14):144103.

[43] Kulakova L, Arampatzis G, Angelikopoulos P, et al. Data driven inference for the repulsive exponent of the lennard-jones potential in molecular dynamics simulations. Scientific reports. 2017;7(1):1–10.

[44] Zavadlav J, Arampatzis G, Koumoutsakos P. Bayesian selection for coarse-grained models of liquid water. Scientific reports. 2019;9(1):1–10.

[45] Keaveny EE, Pivkin IV, Maxey M, et al. A comparative study between dissipative particle dynamics and molecular dynamics for simple-and complex-geometry flows. The Journal of chemical physics. 2005;123(10):104107.

[46] Plimpton S. Fast parallel algorithms for short-range molecular dynamics. Journal of Computational Physics. 1995;117(1):1–19.

[47] Pivkin IV, Karniadakis GE. Coarse-graining limits in open and wall-bounded dissipative particle dynamics systems. The Journal of chemical physics. 2006;124(18):184101.

[48] Martin MG, Siepmann JI. Transferable potentials for phase equilibria. 1. united-atom description of n-alkanes. The Journal of Physical Chemistry B. 1998;102(14):2569–2577.

[49] Jorgensen WL, Madura JD, Swenson CJ. Optimized intermolecular potential functions for liquid hydrocarbons. Journal of the American Chemical Society. 1984;106(22):6638–6646.

[50] Takaishi Y, Oguchi K. Measurements of the density for n-heptane for pressures up to 100 mpa by using a vibrating-wire densimeter. The Review of High Pressure Science and Technology. 1998;7:1192–1194.

[51] Rolo LI, Caco AI, Queimada AJ, et al. Surface tension of heptane, decane, hexadecane, eicosane, and some of their binary mixtures. Journal of Chemical & Engineering Data. 2002;47(6):1442–1445.

[52] Pensado AS, Comuñas MJP, Lugo L, et al. Experimental dynamic viscosities of 2, 3-dimethylpentane up to 60 mpa and from (303.15 to 353.15) k using a rolling-ball viscometer. Journal of Chemical & Engineering Data. 2005;50(3):849–855.

[53] Moore JW, Wellek RM. Diffusion coefficients of n-heptane and n-decane in n-alkanes and n-alcohols at several temperatures. Journal of Chemical and Engineering data. 1974; 19(2):136–140.

[54] Iwahashi M, Yamaguchi Y, Ogura Y, et al. Dynamical structures of normal alkanes, alcohols, and fatty acids in the liquid state as determined by viscosity, self-diffusion coefficient, infrared spectra, and 13cnmr spin-lattice relaxation time measurements. Bulletin of the Chemical Society of Japan. 1990;63(8):2154–2158.

[55] Pan C, Hilpert M, Miller CT. Pore-scale modeling of saturated permeabilities in random sphere packings. Physical Review E. 2001;64(6):066702.

[56] Harvey AH. Thermodynamic properties of water: Tabulation from the iapws formulation 1995 for the thermodynamic properties of ordinary water substance for general and scientific use. US Department of Commerce, Technology Administration, National Institute of . . . ; 1998.

[57] Vargaftik NB, Volkov BN, Voljak LD. International tables of the surface tension of water. Journal of Physical and Chemical Reference Data. 1983;12(3):817–820.

[58] Harris KR, Woolf LA. Temperature and volume dependence of the viscosity of water and heavy water at low temperatures. Journal of Chemical & Engineering Data. 2004; 49(4):1064–1069.

[59] Gillen KT, Douglass DC, Hoch MJR. Self-diffusion in liquid water to- 31 c. The Journal of Chemical Physics. 1972;57(12):5117–5119.

[60] Pivkin IV, Karniadakis GE. A new method to impose no-slip boundary conditions in dissipative particle dynamics. Journal of Computational Physics. 2005;207(1):114–128.

[61] Li Z, Bian X, Tang YH, et al. A dissipative particle dynamics method for arbitrarily complex geometries. Journal of Computational Physics. 2018;355:534–547.

[62] Zhang D, Shangguan Q, Wang Y. An easy-to-use boundary condition in dissipative particle dynamics system. Computers & Fluids. 2018;166:117–122.

[63] Xu S, Wang Q, Wang J. A new wall model for slip boundary conditions in dissipative parti-

cle dynamics. International Journal for Numerical Methods in Fluids. 2019;90(9):442–455.